Acta Astronautica 208 (2023) 343–354

Contents lists available at ScienceDirect

Acta Astronautica

journal homepage: www.elsevier.com/locate/actaastro

Research paper

Unveiling the mechanics of lunar regolith erosion through analysis of CE-4 and CE-5 landing images and fluid simulation

Jilin You [a,b], Xiaoping Zhang [a,b,*], Hsinchen Yu [a,b], Haiyan Zhang [c,h], Cunhui Li [c,g,**], Roberto Bugiolacchi [a,b], Yi Xu [a,b], Yi Wang [c], Pengwei Luo [a,b], Liping Chen [d,***], Baogui Zhang [e], Yingqiao Xu [d], Yongfu Hu [e], Tong Wang [d], Yuming Wang [g], Qingfei Fu [f], Yupeng Gao [f], Weidong Wang [h], Qijun Zhi [i], Linping Feng [j], Haiwen Liu [j], Yifei Cui [k], Jiayan Nie [k]

[a] State Key Laboratory of Lunar and Planetary Sciences, Macau University of Science and Technology, Macau 999078, China
[b] CNSA Macau Center for Space Exploration and Science, Macau 999078, China
[c] Science and Technology on Vacuum Technology and Physics Laboratory, Lanzhou Institute of Physics, Lanzhou 730000, China
[d] Beijing Institute of Spacecraft System Engineering, China Academy of Space Technology, Beijing 100094, China
[e] Beijing Institute of Space Mechanics and Electricity, China Academy of Space Technology, Beijing 100094, China
[f] School of Astronautics, Beihang University, Beijing 100191, China
[g] School of Earth and Space Sciences, University of Science and Technology of China, Hefei 230026, China
[h] School of Mechano-Electronic Engineering, Xidian University, Xi'an 710071, China
[i] School of Physics and Electronic Science, Guizhou Normal University, Guiyang 550001, China
[j] School of Electronic and Information Engineering, Xi'an Jiaotong University, Xi'an 710049, China
[k] State Key Laboratory of Hydroscience and Engineering, Tsinghua University, Beijing 100084, China

ARTICLE INFO

Keywords:
Lunar regolith sample
Mechanical property
Plume–dust interaction
Erosion mass
Erosion model

ABSTRACT

During landing, the plume from the lander erodes the regolith on the lunar surface, thus destroying the nature of this surface. Landing also provides an opportunity to extract the mechanical properties of the lunar regolith *in situ* and to study wind erosion on airless bodies such as the Moon. Our goal in this study is to quantify the interparticle force of the lunar regolith, the erosion depth, and other parameters and to test the reliability of the plume erosion model. The erosion depth provides the necessary reference information for the precise interpretation of scientific results obtained from returned samples. We measure the total mass of the lunar regolith mobilized by the plume during the Moon landing. This information is also helpful for future lunar missions. With high-quality data from the Chang'E-5 (CE-5) and Chang'E-4 (CE-4) missions, we measure the erosion depth and the total mass and combine the results with computational fluid dynamics (CFD) to extract the interparticle force. We then test the plume erosion model according to the results from image measurement and CFD and propose a new formula with which to calculate the threshold friction velocity at which plume erosion is initiated. This calculation shows that the interparticle force for a 4-μm-diameter particle is 3.38–16.1 nN. The results also show that the CE-5 landing plume stripped away a 1.2-cm-deep layer of regolith, creating a ≈10-m-diameter crater on the lunar surface, and dispersed ≈441 kg of lunar regolith. Any analysis of a CE-5 drilling sample that is sensitive to the regolith depth must consider this 1.2-cm-thick eroded layer. When a plume erodes the lunar surface, the minimum shear stress required is much less than that predicted by the erosion model, which can no longer be used to predict whether erosion will occur.

1. Introduction

On December 1, 2020, China's CE-5 lander touched down on the northern Oceanus Procellarum (at 43.06°N, 51.92°W, about 170 km ENE of Mons Rümker) and returned 1731 g of lunar regolith samples. The CE-5 mission is the first return mission of lunar samples since 1976. The CE-5 landing zone is characterized by flat terrain [1] and a thin lunar crust [2]. It is the youngest sampled area on the Moon, with a laboratory sampled age of 2030 ± 4 Ma [3]. The samples and the corresponding magma sources are not as rich in radioactive elements

* Correspondence to: Macau University of Science and Technology, Avenida Wai Long, Taipa, Macao, China.
** Correspondence to: 100 Feiyan Street, Chengguan District, Lanzhou City, Gansu Province, China.
*** Corresponding author.
E-mail addresses: xpzhangnju@gmail.com (X. Zhang), licunhui@spacechina.com (C. Li), chenlipingzs@sina.com (L. Chen).

https://doi.org/10.1016/j.actaastro.2023.04.024
Received 9 November 2022; Received in revised form 4 March 2023; Accepted 13 April 2023
Available online 21 April 2023

as expected [4]. In addition, the mantle source of basaltic volcanism is water-poor [5].

During the CE-5 landing, the plume from the lander interacted with the lunar surface, destroying the nature of this surface. This interaction involves the process of the rocket plume impacting and eroding the lunar surface. Due to the high-vacuum environment on the lunar surface, the exhaust continuously expands after exiting the nozzle and therefore takes the form of a plume. In this interaction, the plume can eject objects on the lunar surface, such as lunar regolith and rocks, and create a crater near the plume impingement point. Unlike wind erosion in an atmospheric environment, these objects usually rapidly escape from the impingement zone along a radial path.

Following the landing, the surface below the craft was sampled. Since the topmost regolith had been stripped away by the exhaust gases, the precise depth of these CE-5 samples remains unclear. However, in terms of studying sample characteristics related to depth, such as determining particle diameter, density, and void ratio, one must consider the thickness of the removed layer. To account for space weathering of exposed materials, this thickness also needs to be considered. For example, the visible-near-infrared reflectance spectra and the submicroscopic metallic iron abundances within the lunar regolith vary with depth [6]. Future lunar missions also require quantitative information about plume erosion, such as the thickness, range, and regolith mass modified by the plume. The goal of this study is to quantify the lunar regolith erosion parameters during the CE-5 landing phase and provide the necessary reference information for the precise interpretation of scientific results obtained from returned samples.

Five Surveyor spacecraft [7] measured *in situ* the mechanical properties of the lunar surface materials. The cohesion and friction angle of particulate material at a depth of a few centimeters are about 500 Pa and nearly 40°, respectively; the top millimeter has a slightly lower cohesion (300 Pa). Roberts [8] proposed viscous erosion theory in 1963 and Metzger et al. [9] improved it in 2008, more recent works [10–12] have used this improved model to study plume–lunar surface interactions. Alternatively, Lane et al. [13] used Sagan's formula [14] to analyze the erosion of the lunar surface by the Apollo 12 plume. In this paper, we extract the mechanical parameters of the topmost lunar regolith *in situ* at the CE-4 landing site. This extraction is vital for determining the mechanical parameters of the lunar regolith in subsequent landing missions. In addition, we will verify *in situ* the feasibility of the viscous erosion theory in the interaction between the plume and the lunar surface.

Since erosion depends on various conditions such as the lander thrust, landing method, regolith mechanic properties, and local topography, we cannot accurately model this process due to its internal complexities and uncertain parameters. It is also hard to reproduce in the laboratory the same thrust, near-vacuum boundary conditions, and similar regolith mechanical properties at the CE-5 landing site. Therefore, we must measure regolith erosion *in situ* based on images captured during the descent of the CE-5 lander. Both the field of view and the resolution of the CE-5 landing camera are optimized compared with the Apollo and CE-4 missions, which allows us to calculate higher-precision regolith erosion parameters in addition to the regolith mechanical parameters.

Until now, no measurement existed of the crater's shape nor of the total mass of the lunar regolith eroded by the plume during landing. In this study, we measure the crater's shape, erosion mass, and other erosion parameters based on CE-5 landing images. The results are helpful to the scientific study of CE-5 samples and to future sampling tasks; in addition, they provide new insights for erosion theory. We also propose a formula for the threshold velocity of plume erosion during descent, which helps the analysis of plume erosion.

2. Data and methods

2.1. CE-5 landing images

The CE-5 landing camera was installed on the bottom of the lander [see Fig. 1]. This camera operated from 499 s before landing until 134 s after landing. It has two working modes: In mode 1, it continuously outputs five images every 5 s, with 2352 × 1728 pixels. In mode 2, it outputs one image per second, with 1024 × 1024 pixels. These two modes operate alternately. The landing camera captures over 600 images during the CE-5 mission.

The landing images of CE-5 have been radiometrically corrected and are available online [15]. In this paper, we analyze only the landing images obtained via mode 1. All landing images of CE-5 are grayscale images. The image brightness is divided into 256 levels: 0 represents the lowest intensity, and 255 represents the highest intensity. The exposure time of the landing images is divided into four windows: 4.5, 3.23, 2.32, and 2.22 ms. For subsequent analysis, we obtained the equivalent radiation of the images as follows: first, we derived a linear function by fitting the digital number and the corresponding equivalent radiation measured in the laboratory for different exposure times. The related data are listed in Supplementary Table S3. We then used this function to calculate the equivalent radiation of any digital number in the landing image.

Fig. A.1 in Appendix A shows the mean equivalent radiance of the landing image for the final 49 s of descent. The image brightness remains constant before −30 s and then decreases slightly around −20 s due to a large shadow from the crater in the shooting area. After −7 s, the brightness rises rapidly and peaks at −1 s because dust appears on the lunar surface. Finally, the number density of the dust also peaks at −1 s. A detailed description of the dust ejection patterns is available in Appendix A.

2.2. Simulation of plume–lunar-surface interaction

We adopt the direct simulation Monte Carlo method (DSMC) proposed by Bird [17] to simulate the interaction between the engine exhaust and the lunar surface. The DSMC method treats the flow field as a series of discrete molecules, which is suitable for simulating rarefied gas flows. The computational domain of the DSMC method is shown in Fig. 2, and the simulated altitudes of the CE-5 and CE-4 nozzles are listed in Supplementary Table S4. The length of the lunar surface in Fig. 2 is 10 m. The lunar surface and the wall are treated as fully diffuse boundaries at 300 K. The entire computational domain consists of a series of $0.01\ \text{m} \times 0.01\ \text{m}$ grids.

The DSMC method treats the gas flow field as consisting of individual molecules. Due to a large number of real molecules, one simulated molecule in the DSMC method represents many real molecules. In our simulations, one simulated molecule represents 5×10^{15} real molecules. The collision cross section between simulated molecules uses a variable hard-sphere model [17], and the corresponding viscosity index and reference temperature are taken as 0.75 and 273 K, respectively. Our simulations consider the rotational degrees of freedom of the gas but not the vibrational degrees of freedom. The dynamic viscosity of the gases is computed by using Sutherland's law. During the execution of the DSMC program, the time step of the simulation is $0.5\ \mu\text{s}$.

The DSMC output is the statistical result of the computational molecules in the computational cells. For example, the total number density is $\rho_n = \sum_p n_p$, where n_p is the number density of gas molecules of species p, which equals the number of computational molecules of species p times the number of real molecules represented by a computational molecule volume divided by a grid cell volume in the DSMC simulation.

The accuracy of the DSMC output is determined by whether the number of computational molecules in the DSMC simulation suffices to approximate the evolution of the statistical state of the real molecules.

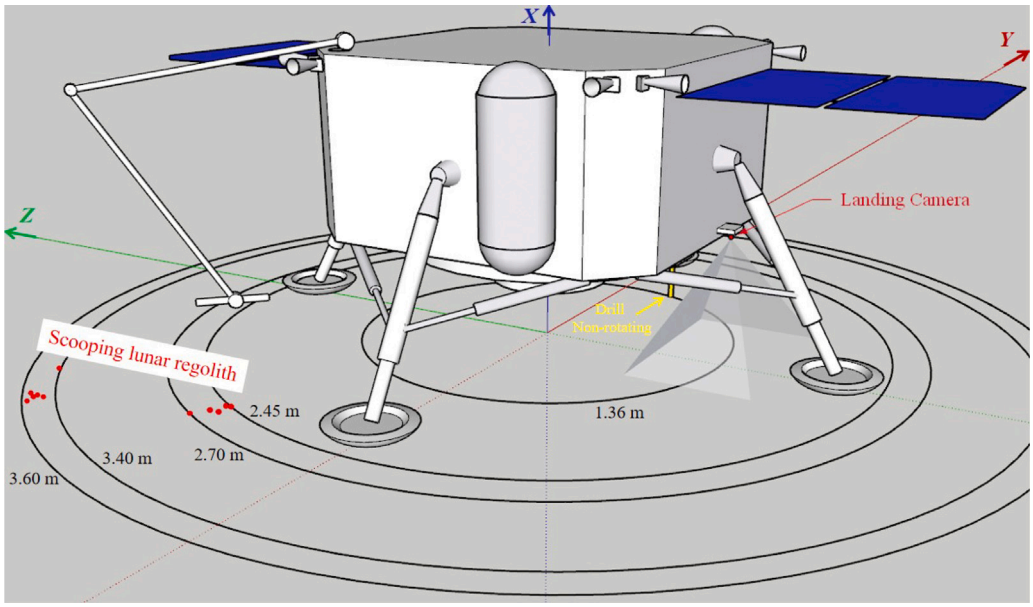

Fig. 1. Schematic diagram of CE-5 lander. The optical axis of the landing camera is in the vertical direction. The camera's altitudes and parameters are listed in Supplementary Tables S1 and S2, respectively. The locations (red dots) where lunar regolith was scooped are from Zheng et al. [16]. The X axis coincides with the nozzle axis, and the Y and Z axes are shown in the plane of the footpads.

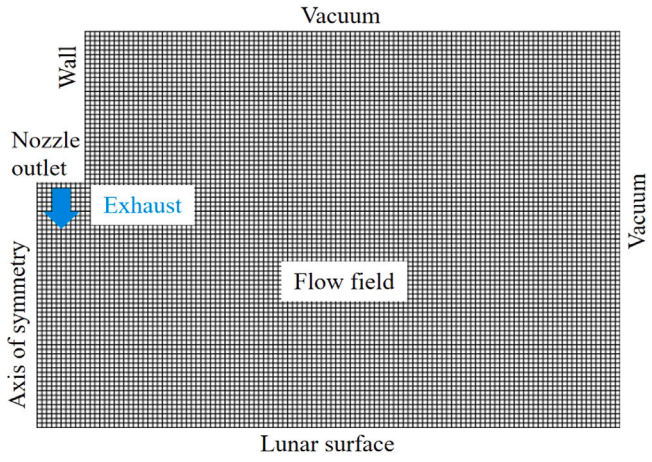

Fig. 2. Schematic diagram of meshes and boundaries used for simulation.

At the same time, the cell size and the time step also influence the DSMC output. The cell size should be larger than the gas molecules' mean free path, and the simulation time step should be shorter than the mean free path of the gas molecules divided by the mean thermal velocity of the molecules. Given these conditions, the decoupling of the molecular motions from molecular collisions during a time step in the DSMC is reasonable.

3. Results and discussion

3.1. Erosion depth of lunar regolith

As the CE-5 craft approached its landing target, the exhaust gases scattered the loose surface materials. The thickness of the removed layer is defined as the erosion depth of the lunar regolith. Fig. 3(a) shows some regions on the lunar surface marked with red boxes. The regolith at these positions is raised and forms a regolith bulge. In addition, the corresponding shadows appear to the lower left of these regolith bulges due to illumination by the Sun. The bulges in Fig. 3(b) are almost flattened by the exhaust. Consequently, we regard the thickness of these bulges as the erosion depth of the lunar regolith during this landing period. Fig. 3(c) shows the erosion depth based on the measurement of the bulge thickness; the details of this thickness calculation appear in Appendix C. The corresponding erosion time ranges from 4 s before landing to 1 s after landing [Fig. 3(c)]. The corresponding nozzle altitude ranges from 7.83 to 0.46 m. Fig. 3(c) reveals no obvious correlation between the erosion depth and the distance from the nozzle centerline, which is also shown in Fig. 3(d). This result may be due to the small measured area ($\approx 1.1 \times 0.8$ m^2) compared with the size of the overall crater.

From Fig. 3(c), the erosion depth is between ≈0.8 and ≈1.8 cm, with an average depth of 1.2 ± 0.1 cm. This average value is 1.7 times the erosion depth caused by the CE-4 engine [18]. The difference in erosion depth is caused by several factors: first, the thrust of the CE-5 engine is 2900 N, which is about 700 N greater than that of the CE-4 engine. Second, the erosion depth (1.2 ± 0.1 cm) of CE-5 corresponds to an erosion time of 5 s, which is 3.3 times that of CE-4. The difference in erosion depth may also be partly caused by the regolith properties, although the contribution of these factors to the difference in erosion depth is unclear. The effect of different factors on erosion depth should be further studied via numerical models. Here, we do not consider the influence of erosion area and the distance to the nozzle axis because these two quantities for CE-5 are close to those of CE-4. The measurement area of CE-5 is $\approx 1.1 \times 0.8$ m^2, and the center of this area is ≈1.6 m from the nozzle axis [see Fig. 3(c)]. For CE-4, these two values are $\approx 0.9 \times 0.7$ m^2 and ≈1.5 m, respectively.

Some artifacts or errors should be avoided when identifying features such as bulges in the image. During landing, the CE-5 lander has a nonzero horizontal speed with respect to the lunar surface, which will affect the images acquired by the landing camera. For example, the horizontal velocity associated with image F414 is 0.0127 m/s, so a 0.04 mm smear appears in the image with an exposure time of 3.23 ms. However, this length scale is much less than the 4 mm resolution of image F414. Therefore, the horizontal movement does not seriously affect the quality of image F414 and thus should not affect our identification of soil bulges in Fig. 3 and the corresponding calculations.

When choosing soil bulges, care must be taken not to misidentify rocks as soil bulges. For example, the color of the soil bulges in Fig. 3(a) is close to that of the surrounding soil. An object in the image that

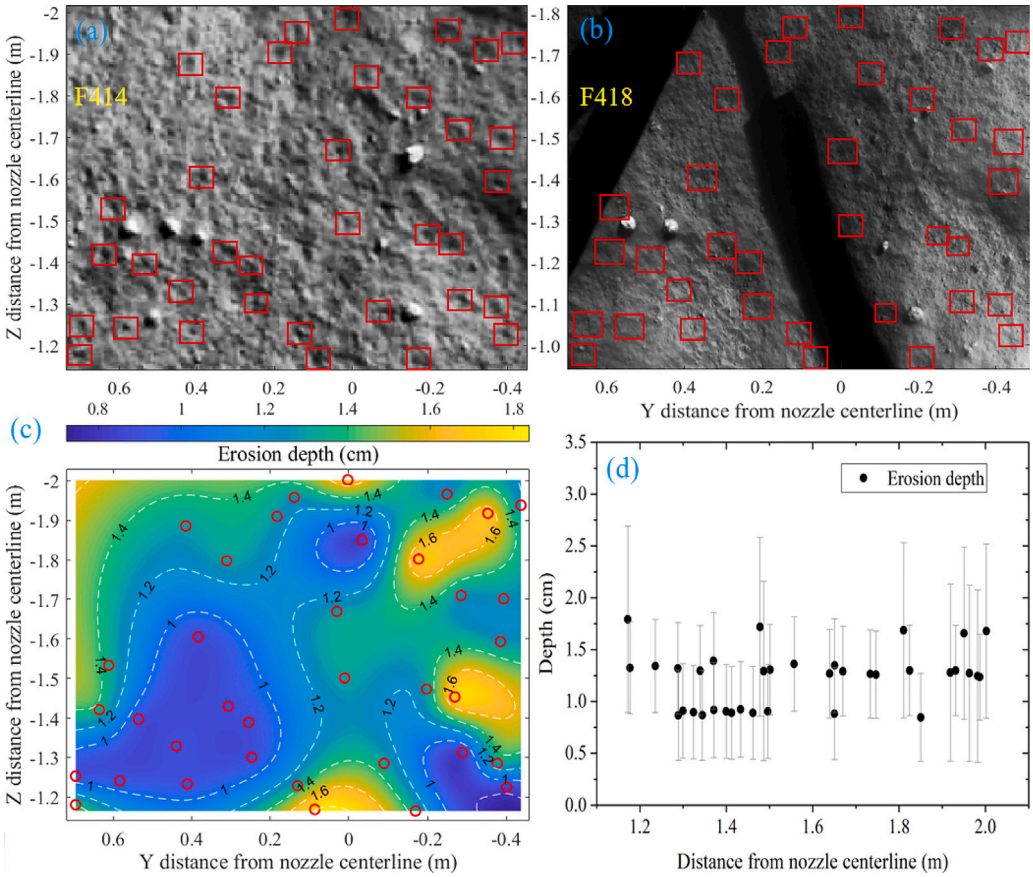

Fig. 3. Measurements of erosion depth due to the plume on the lunar surface. (a), (b) Comparison of terrains in the same area before and after landing. The image at touchdown is F417. The red boxes' in panels (a) and (b) are in a one-to-one correspondence. The contrast between F414 and F418 is enhanced. (c) Measured erosion depth of lunar regolith based on panels (a) and (b). This map is obtained by interpolation between the values measured at the red circles. The red circles are in a one-to-one correspondence with the red boxes in panel (a). (d) Variations of measured erosion depths as a function of distance from nozzle centerline.

appears as a bright spot with a very clear outline is probably a rock. If the object cannot be recognized, it is eliminated to avoid possible errors. In addition, we avoid analyzing bulges whose shadow width occupies only one pixel because this can lead to large calculation errors.

3.2. Erosion mass of lunar regolith

The erosion mass here refers to the total erosion mass of lunar regolith that is blown away by engine exhaust during landing. Estimating the erosion mass requires measuring the minimum $r_{0\min}$ of the erosion radius throughout the landing process, where r_0 is the radius centered on the nozzle axis, and the lunar regolith at r_0 is blown away by the engine plume. The lunar regolith does not rise from the flat lunar surface within the radius r_0 (see Table A.1 for an illustration of r_0). The radius r_0 for the CE-5 lander when it just touches the ground is its minimal value for the entire descent. However, due to the limited observation angle, the CE-5 landing camera cannot image this $r_{0\min}$. We thus measure r_0 by using the image 1 s before the CE-5 lander touches down. We plot two red lines in image F416 (see Table A.1). The red line on the left is on the outline of the dust streak, and the red line on the right is on the corresponding shadow of this outline. The intersection of these two red lines is where the dust just rises. According to image measurements, this intersection is 0.23 m from the nozzle axis. We take the erosion depth at $r_0 = 0.23$ m as zero and merge it into the data of erosion depth in Fig. 4.

To calculate the total mass of the lunar regolith mobilized by the CE-5 engine, we first fit the erosion depth $D_e(r)$ profile in Fig. 4 by the empirical formula

$$D_e(r) = 0.01\left(\frac{c_1}{r^{p_1}} - \frac{c_2}{r^{p_2}} + c_3\right). \quad (1)$$

Here, the radius r is the distance from the nozzle axis. Both the radius r and $D_e(r)$ are in meters. The corresponding fitting parameters c_1, c_2, c_3, p_1, and p_2 are 239 639.388 38, 239 625.361 57, −12.664 38, 0.305 276, and 0.305 293, respectively.

Next, we substitute these fitted parameters into Eq. (1) to obtain the shape of the crater formed due to erosion (see the red curve in Fig. 4). Finally, the total erosion mass M_T is calculated by

$$M_T = \rho_{lr}\int_{r_0}^{a_0} 2\pi r D_e(r)dr, \quad (2)$$

where the lunar regolith density ρ_{lr} at the CE-5 landing site is 1238.7 kg/m^3 [19], $r_0 = 0.23$ m, and the erosion depth within a radius of $r_0 = 0.23$ m is assumed to be zero when calculating M_T. The maximum erosion radius $a_0 = 4.65$ m is determined in the fitting process from the previous paragraph. Substituting Eq. (1) and the corresponding parameters into Eq. (2), we get $M_T = 441$ kg for $0.23\ \text{m} \le r \le 4.65$ m.

The erosion mass fractions in Ranges I–III are about 10.4% (46 kg), 30.4% (134 kg), and 59.2% (261 kg), respectively. Although the erosion depth in Range III is relatively small, Range III covers an erosion area of 82%, making it the largest erosion-mass fraction.

Large uncertainties exist in the current erosion-mass estimation within Range III. Due to the limited field of view of the landing camera, erosion depths in Range III correspond to erosion times ranging from −4 s to −3 s. The erosion period is only 1 s, which accounts for only 1/7 of the dust-ejection period before landing. This implies that the erosion depth in Range III of Fig. 4 represents only a part of the total erosion depth in the whole landing process. If we consider the total erosion depth, we obtain a larger erosion mass for Range III.

Alternatively, our method may overestimate the total erosion mass: here, we used the erosion depth measured from Fig. 4. These erosion

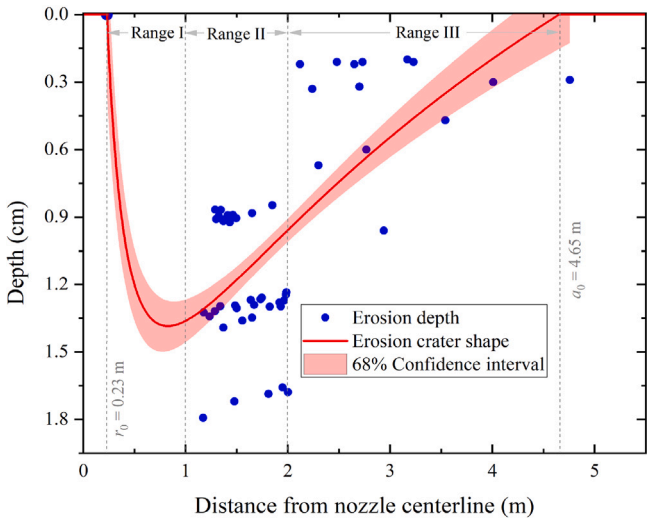

Fig. 4. Erosion depths as a function of distance from nozzle centerline. The measured values in Range II and the range 2–5 m are obtained from Fig. 3(d) and Appendix D, respectively. The data point (0.23 m, 0 cm) is inferred from image F416 of CE-5. The derivation process is explained in the first paragraph of Section 3.2. Eq. (1) is fit to the shape of the erosion crater.

depths are calculated based on the thickness of the bulge on the lunar surface. Three types of local topography with area A_e are possible on the observed lunar surface: raised, flat, and low lying. The erosion thickness at the raised location (bulge) is the largest among the three terrains because the plume from the engine almost flattened the bulge. The plume at the latter two terrains is relatively weak. In theory, due to the highest topography at the bulge, the shear stress of the same airflow is also maximal, resulting in the largest erosion thickness. The erosion depth associated with the latter two terrains cannot be larger than that of the bulge. In the calculation, we multiply the erosion area A_e by the measured variation in bulge thickness to obtain the erosion volume, which could be larger than the actual erosion volume. This could also result in an overestimate of the total erosion mass. A more accurate estimation requires measuring the change in the elevation of the landing zone during the landing process.

3.3. Interparticle force of lunar regolith

As the engine's plume erodes the lunar surface, lunar dust begins to rise from a specific position r_0. The initiation process of lunar dust particles at r_0 is divided into two processes [Fig. 5]. The first is the static friction between particles [Figs. 5(a) and 5(b)], and the second is the rotation of the particles [Fig. 5(b)–5(d)]. In the first process, the drag F_d continues to increase until it balances the horizontal component of F_{CA} and $F_{BA} = 0$. At this time, particle A is in a critical static equilibrium state [Fig. 5(b)]. After entering the second process, F_d increases again. The net torque experienced by particle A is no longer zero [Fig. 5(c)], so particle A rotates clockwise about point P. Finally, particle A breaks away from the bottom particle and enters the flow field [Fig. 5(d)].

In the following, we estimate the interparticle force between particles at the critical static equilibrium state. Li et al. [19] measured the particle sizes for the CE-5 lunar regolith range from 1.11 to 499.80 μm, and 95% of the particles are distributed between 1.40 and 9.35 μm, with a mean of 3.96 μm. Therefore, we here take this typical diameter of 4 μm to calculate the interparticle force of the CE-4 lunar regolith. The interparticle force F_i can be fit by Eq. (E.2) with $k = \sqrt{3}$ for three tangent spheres with equal diameters [see Fig. E.1(c)]. The corresponding fitting formula from Eq. (E.2) is

$$\frac{1}{2}\rho_g u_*^2 = f\left(Re_*\right)\left[\left(\frac{1}{2}\rho_p g d + \frac{3}{4}\Delta P\right) + 3\sqrt{3}\frac{F_i}{\pi d^2}\right], \tag{3}$$

where ρ_p is the density of a particle (3195.2 kg/m^3 [19]). Below we calculate the range of the interparticle force F_i. When ΔP in Eq. (3) takes the maximum value P_d, the interparticle force is minimal: $F_{i,min}$. We then fit the dynamic pressure versus P_d at r_0 for CE-4 by using Eq. (3) with the typical dust diameter from the CE-5 landing site, d = 4 μm [Fig. 6] [19]. The corresponding fitting parameters are $F_{i,min}$ = 3.38 ± 0.40 nN and $f(Re_*)$ = 0.026 ± 0.0015. The interparticle forces for particles with other diameters can be obtained by the same fitting process.

When ΔP in Eq. (3) decreases to zero, the corresponding interparticle force reaches the maximum value, $F_{i,max}$. Eq. (3) with $\Delta P = 0$ is equivalent to Eq. (E.1) of Shao and Lu [20]. We substitute $f(Re_*)$ = 0.0123 fitted by Shao and Lu [20] and $\Delta P = 0$ into Eq. (3). From Eq. (3), one can then derive $F_{i,max}$ = 16.1 nN for particles with a diameter of 4 μm when the dynamic pressure of the plume is equal to ≈20.5 Pa from Fig. 6. To sum up, after considering the plume pressure at the bottom of the particle, the interparticle force is in the range 3.38–16.1 nN for 4-μm-diameter particles. The ratio of 3.38–16.1 nN to π(2 μm)^2 implies a cohesion of 269–1281 Pa between 4-μm-sized particles on the topmost CE-4 regolith. This cohesion range is consistent with the value of 300 Pa for the top millimeter of lunar regolith obtained by Surveyor tests [7].

The interparticle force between two smooth, contacting 4-μm-diameter spheres is 0.25–25 μN from Eq. (8) by Walton [21] with a typical surface energy of 20–2000 mJ/m^2. In contrast, our estimated value (3.38–16.1 nN) is 1–4 orders of magnitude smaller than that predicted by Walton's equation. If the surface energy of lunar regolith particles is two orders of magnitude smaller than 20–2000 mJ/m^2, the prediction of Walton's equation would be close to our estimate. However, Walton [21] explains that the attractive force between particles is sensitive to the roughness of the particle surface; when the surface roughness of the particle is at least 10 nm, the effective attraction at contact decreases by at least an order of magnitude. Most lunar regolith particles are irregular in shape and have a certain surface roughness. This argument likely explains why our estimated interparticle force for lunar regolith based on an ideal smooth sphere is lower than Walton's prediction.

In Fig. 6, we only used r_0 and the corresponding fluid data from CE-4 and did not use those of CE-5. The CE-4 landing camera has an exposure time of 0.1 s, which is ten times faster than the CE-5 landing camera. The CE-4 landing camera can export more images, so r_0 measured from these images is more accurate. In addition, the interparticle force between particles is only related to the particle type and diameter. Therefore, using the interparticle force derived from the CE-4 data as a reference will not cause a significant error.

3.4. Views on current plume erosion during landing process

In Section 3.3, we extract the mechanical parameters of lunar regolith based on an analysis of the force exerted on individual regolith particles. Likewise, previous studies [13,14,20] used a similar method to analyze the dust initiation. In contrast, some previous studies considered a mass of surface regolith as the object of analysis and assumed it to be sheared by the plume with the dynamic pressure $C_d\rho_g u^2/2$, where the drag coefficient C_d = 1, ρ_g is the gas density, and u is the gas velocity. Similar processes have persisted in recent plume erosion studies [10–12] since Metzger et al. [9] improved upon Roberts' original viscous erosion theory [8]. These articles also hold a common view: viscous erosion occurs when the plume shear stress (using the local dynamic pressure $\rho_g u^2/2$) exceeds the threshold stress ($C + P_d \tan\phi$) of the lunar regolith. Here, C, P_d, and ϕ are the regolith cohesion, downward pressure of the plume on the lunar surface, and friction angle of the regolith, respectively.

According to this view and assuming P_d = 600 Pa, the measured values of C = 300 Pa [7] and ϕ = 42° [22], one needs a plume shear stress of 840 Pa to move the lunar regolith. However, Fig. 6 shows that

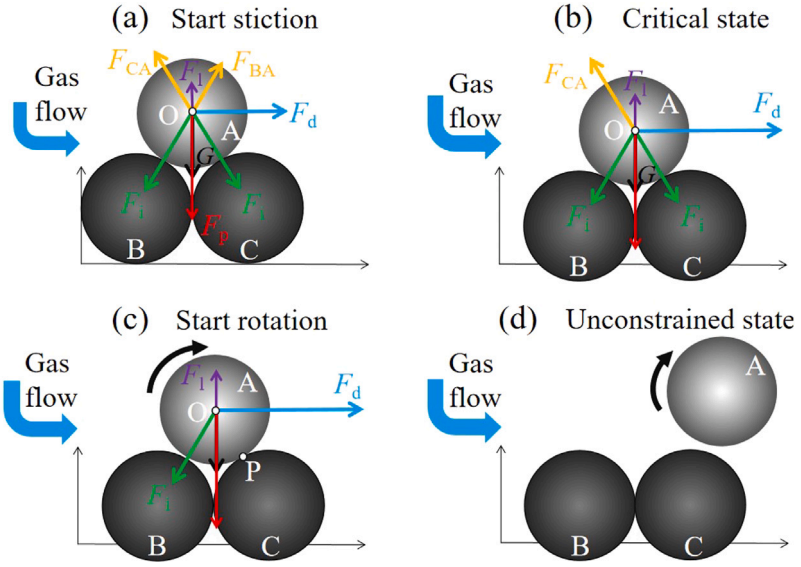

Fig. 5. Initiation process of particle at position r_0. (a) Particle A on top starts to rub against particles B and C due to the forces. The forces exerted on the particle center O of mass include the interparticle force F_i, drag F_d, lift F_l of the gas flow, particle gravity G, pressure F_p of the gas flow, and the normal forces F_{CA} and F_{BA}. (b) Particles A, B, and C are squeezed by the gas flow. Particle A is in a critical static equilibrium state and just about to rotate. (c) Particle A starts to rotate about point A under the action of gas flow. (d) Particle A breaks away from the shackles of the bottom particles and enters the airflow field. Each arrow in panels (b) and (c) has the same meaning as in panel (a).

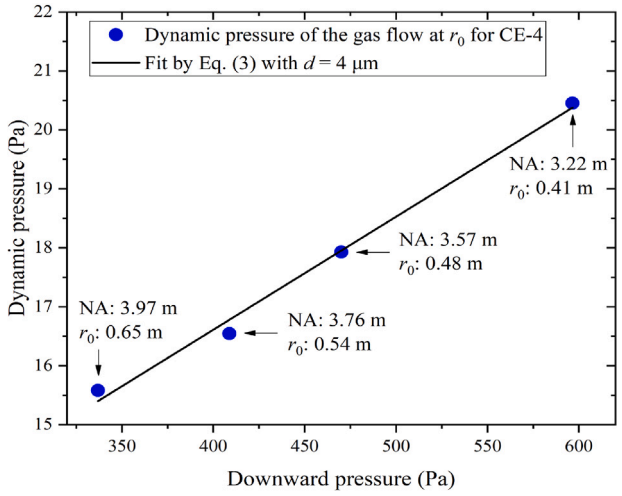

Fig. 6. Dynamic pressure versus downward pressure of the gas flow at r_0 for CE-4. Dynamic pressure and downward pressure are obtained from the DSMC method of Section 2.2. The selected location of the gas flow is 0.7 cm above the lunar surface in the DSMC method, which represents the average height of the regolith bulge in the CE-4 landing zone. "NA" is the nozzle altitude of the engine with respect to the lunar surface.

the local dynamic pressure of ≈20.5 Pa at P_d = 600 Pa just suffices to move the lunar regolith. This value is 41 times smaller than that of 840 Pa. According to Eq. (3) and Fig. 6, a single particle can be moved by gas flow with dynamic pressure of ≈20.5 Pa. Before the dynamic pressure reaches 840 Pa (the stress required for a mass of regolith to slip), a large number of particles have been blown away by the plume. Therefore, the assumption that a large number of particles can be treated as a whole is unreasonable, so the threshold stress from Roberts' theory should not be used to judge whether viscous erosion occurs [8]. According to the present study, one can determine whether viscous erosion occurs from the threshold velocity given by Eq. (4) or similar equations:

$$u_*^2 = f\left(Re_*\right)\left[\left(\sigma_p g d + \frac{3\Delta P}{2\rho_g}\right) + k\frac{6F_i}{\pi\rho_g d^2}\right]. \quad (4)$$

The physical meaning and origin of this formula are explained in Appendix E. Conversely, if Roberts' theory holds, then local dynamic pressure $\rho_g u^2/2$ equals the threshold stress $C + P_d \tan\phi$ at the critical position r_0. By fitting the data points in Fig. 6 with this equation, one can derive that the regolith cohesion and friction angle are 9 Pa and 1°, respectively. These two values are much smaller than the measured 300 Pa [7] and 42° [22], respectively. The corresponding static friction coefficient is about $(\tan 42°/\tan 1°) \approx 52$ times smaller.

In our calculations, the drag stress on a single particle with a particle diameter of 1–10 μm is $C_d\rho_g u^2/2$. Here, the drag coefficient C_d is between 50 and 61 (the calculation of C_d appears in Appendix F). On the other hand, the shear stress experienced by a mass of regolith equals the local dynamic pressure $\rho_g u^2/2$ from Robert's theory [8]. Here, the stress of the latter is 50–61 times smaller than that of the former, which is why the static friction coefficient derived from the latter is about 52 times smaller than that of the former.

4. Conclusions

Based on landing images obtained from the CE-5 mission, we quantitatively analyzed how plume impingement affects the lunar regolith. The results show that a layer of regolith about 1–2 m from the nozzle axis was stripped off by the 7500 N throttleable engine plume, with an average erosion thickness of 1.2 ± 0.1 cm. Since the CE-5 drilling samples were taken from the above range, this analysis defines a starting depth of ≈1.2 cm below the uppermost layer for the drilling samples. For the CE-5 scooping samples, the starting depths are 0.7 ± 0.06 and 0.4 ± 0.1 cm at around 2.58 and 3.50 m from the nozzle axis, respectively. In addition, we estimate the shape of the erosion crater due to plume impingement. The crater is located 0.23–4.65 m from the nozzle axis and has a maximum depth of 1.4 cm. The lunar regolith mass thrown from this crater is 441 kg.

The depths at which the samples are taken could influence the relationship between the characteristics of the CE-5 samples and the depths. These characteristics include particle diameter, density, void ratio, radiation dose, space weathering, and spectroscopy. In particular, the analysis of the uppermost layer of the regolith sample depends more on an accurate sample depth. The drilling samples of CE-5 are divided according to the casing position and the length of each section is 1.5 cm. If the 1.2-cm-thick regolith stripped by the CE-5 plume is

ignored, the maximum depth of the topmost section of the sample will be underestimated as 1.5 cm, a reduction of ≈1 time. Similarly, the depth of the scooping samples of CE-5 will be underestimated as approximately zero. These underestimates will then affect all conclusions based on the CE-5 samples. For example, the radiation dose received by the uppermost lunar regolith could be underestimated and its radiation history could be misjudged. Therefore, in any analysis related to the sample depth, the stripped thickness of 1.2 cm should be properly considered.

We have also quantified the characteristics of dust emission during the CE-5 landing. When the CE-5 nozzle altitude is ≈13.74 m, dust begins to appear. This altitude is slightly higher than the nozzle altitude of ≈13 m, which is the altitude at which dust appeared below the CE-4 lander. The interparticle force associated with a 4-μm-diameter particle is 3.38–16.1 nN. The result shows that the viscous erosion theory modified by Metzger et al. [9] cannot be applied to plume-erosion studies. Therefore, we propose a new formula for the threshold friction velocity based on the landing images. This formula can be used to predict the gas flow velocity when the particles are just initiated by the plume.

The regolith erosion quantities measured in this paper are important references for future lunar missions. For example, to collect samples without plume erosion, the collection should be done at least 4.65 m from the lander (CE-5-like lander). The measurements (erosion depth, r_0, etc.) provide important references for developing models about the interaction of lander plumes with the lunar surface.

CRediT authorship contribution statement

Jilin You: Software, Validation, Investigation, Writing – original draft, Visualization. **Xiaoping Zhang:** Conceptualization, Methodology, Investigation, Writing – review & editing, Visualization, Supervision, Project administration, Funding acquisition. **Hsinchen Yu:** Software, Validation, Data curation. **Haiyan Zhang:** Software, Validation, Data curation. **Cunhui Li:** Investigation, Resources, Data curation, Supervision, Funding acquisition. **Roberto Bugiolacchi:** Writing – review & editing. **Yi Xu:** Writing – review & editing. **Yi Wang:** Data curation. **Pengwei Luo:** Data curation. **Liping Chen:** Supervision, Project administration. **Baogui Zhang:** Formal analysis. **Yingqiao Xu:** Formal analysis. **Yongfu Hu:** Formal analysis. **Tong Wang:** Formal analysis. **Yuming Wang:** Data curation. **Qingfei Fu:** Data curation. **Yupeng Gao:** Data curation. **Weidong Wang:** Formal analysis. **Qijun Zhi:** Data curation. **Linping Feng:** Formal analysis. **Haiwen Liu:** Formal analysis. **Yifei Cui:** Data curation, Methodology, Investigation. **Jiayan Nie:** Data curation, Methodology, Investigation.

Declaration of competing interest

The authors declare that they have no known competing financial interests or personal relationships that could have appeared to influence the work reported in this paper.

Acknowledgments

Scientific data from the Chang'e missions are provided by the China National Space Administration (CNSA). We are grateful for the support from the team members of the Ground Research and Application System (GRAS), who contributed to data receiving and preprocessing. This work was supported by the Science and Technology Development Fund (FDCT) of Macau [grant numbers 0042/2018/A2, 0014/2022/A1]; the National Natural Science Foundation of China [grant numbers 42004157, 41941001, 11761161001]; the Key Laboratory Fund of Science and Technology on Vacuum Technology and Physics [grant number 6142207200202]; and the Pre-research Project on Civil Aerospace Technologies of CNSA [grant number D020201].

Appendix A. Description of ejected-dust patterns

Table A.1 shows six typical landing images with different ejected-dust patterns acquired during the CE-5 landing. The dust appears when the nozzle altitude is 13.74 m (Image ID: F411). As the altitude decreases, the number density of the dust gradually increases. Finally, the number density of the dust peaks at a nozzle altitude of 1.54 m (Image ID: F416). In image F416, the dust is also organized in a stripe-like pattern.

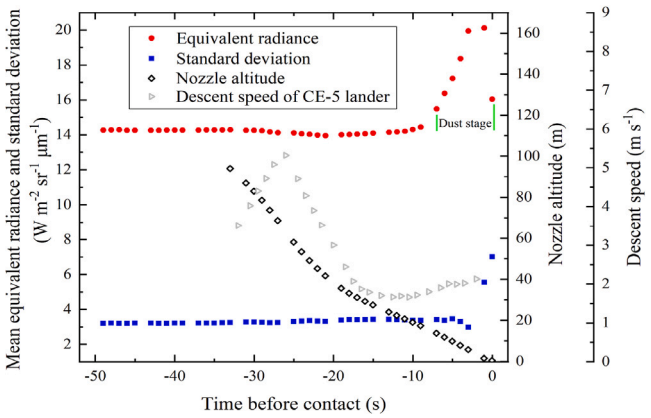

Fig. A.1. Mean equivalent radiance and standard deviation of landing images, nozzle altitude, and descent speed as a function of time before landing. The negative sign on the lower axis indicates the time before landing, and 0 is touchdown. The nozzle altitude and the descent speed are calculated by using the method from Appendix A [18]. The nozzle altitude is listed in Supplementary Table S1.

The various ejected-dust patterns from the CE-5 landing process are similar to those from the CE-4 mission. In the latter, the dust began to appear at a nozzle altitude of ≈13 m, which is close to the altitude extracted from the CE-5 mission. The number density of the dust for CE-4 also increases with decreasing nozzle altitude. As these landers approached the lunar surface, the dust developed into a streaky distribution. In addition, a darker circular area appears under the nozzles of both landers with dust rising from the edge of this circular area. For example, image F414 of Table A.1 shows that most of the lunar dust begins to rise within the radius r_0, where the lunar regolith cannot be moved by the plume. The lunar regolith within radius r_0 is located under the engine nozzle and is subjected to a large normal pressure of the plume. Here, the drag force of the plume cannot overcome the friction force (it is positively related to the normal pressure) and the interparticle force between particles, so the particles within the radius r_0 cannot move. The lunar regolith particles at the radius r_0 are in a critical static-equilibrium state, and the drag force of the plume just overcomes the friction and interparticle force between particles. Therefore, one can use the lunar regolith at r_0 to extract the mechanical parameters of the interaction between particles. For subsequent numerical analysis, we tabulate some of the measured results for r_0 for CE-5 and CE-4 (see Supplementary Table S4).

When the nozzle altitude of CE-5 is 1.54 m (image F416), the number density of dust is relatively high along some radial directions. Similarly, when the nozzle altitude of CE-4 is 1.31 m (image F3369), a large amount of dense lunar regolith suddenly flies out. Several Apollo missions also recorded that such a burst occurred just before the engine shut off [23]. The simulation by Morris et al. [24] indicates that the recirculation bubble in the plume can cause such a burst.

Appendix B. Calculation of solar altitude and azimuth angles

Solar altitude and azimuth angles are used to calculate the height of objects with shadows in the landing images. In addition, these two angles can reflect the slope of the CE-5 landing zone. Below, we use SketchUp software and CE-5 landing images to extract these two angles.

In Fig. B.1(a), the shadow angle of the shock-absorbing rods is measured to be ≈134°. According to this angle and the installation position of the shock-absorbing rods, we simulate the corresponding

Table A.1
Typical landing images from CE-5.

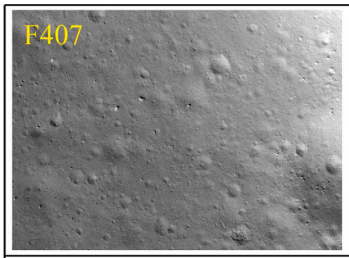	Nozzle altitude: 22.42 m Time before contact: -12 s Exposure time: 4.5 ms In this image, there is no dust on the lunar surface.
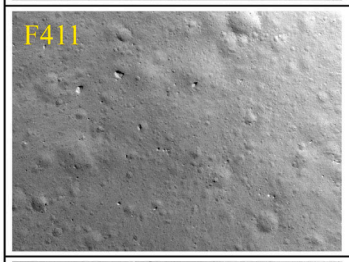	Nozzle altitude: 13.74 m Time before contact: -7 s Exposure time: 4.5 ms The image brightness has increased significantly, and a little dust can be seen in the left half of the image.
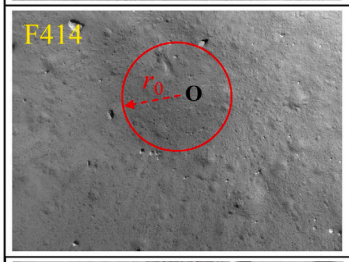	Nozzle altitude: 7.83 m Time before contact: -4 s Exposure time: 3.23 ms A darker area appears within the radius r_0, and most of dust begins to rise from the radius r_0. Point O is located on the nozzle axis.
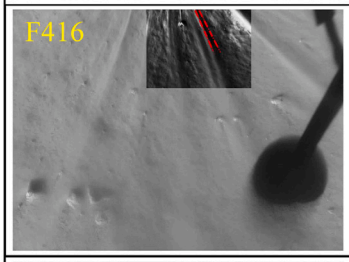	Nozzle altitude: 1.54 m Time before contact: -1 s Exposure time: 2.32 ms The number density of dust is relatively high along some radial directions, and dust tails appear on the edges of the rocks. At this time, the engine has been shut down. The contrast for this image is enhanced.
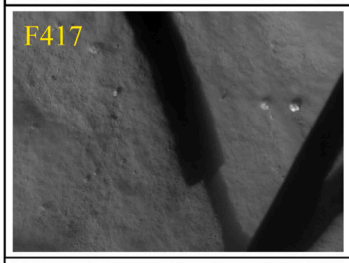	Nozzle altitude: 0.48 m Time before contact: 0 s Exposure time: 2.22 ms A small amount of dust is evenly distributed throughout the field of view. The brightness of the image begins to decrease.
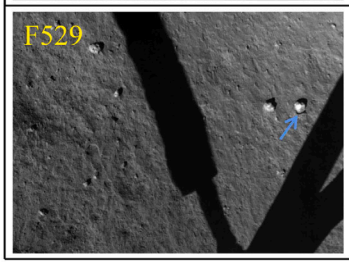	Nozzle altitude: 0.46 m Time after contact: 134 s Exposure time: 2.22 ms The dust has cleared in this image. As indicated by the blue arrow, the stone moved a certain distance due to the influence of the plume.

solar altitude and azimuth angles in the software [Fig. B.1(b)]: the solar altitude and azimuth angles are determined to be 38° and 127.5°, respectively. In the image after landing [Fig. B.2(a)], the same solar altitude and azimuth angles are obtained with the same method.

The solar altitude angle relative to the horizontal is about 37.5° from WebGeocalc [25]. This angle is close to the solar altitude angle of 38° obtained from the CE-5 landing images [Fig. B.1(a) and B.2(a)]. This also implies that the slope of the CE-5 landing zone should be less than 1°, which is a relatively flat surface.

Appendix C. Measurement of erosion depth of lunar regolith

Under the illumination of the Sun [Fig. C.1], a bulge shadow appears in the lower-right corner of the bulge. This scene was captured

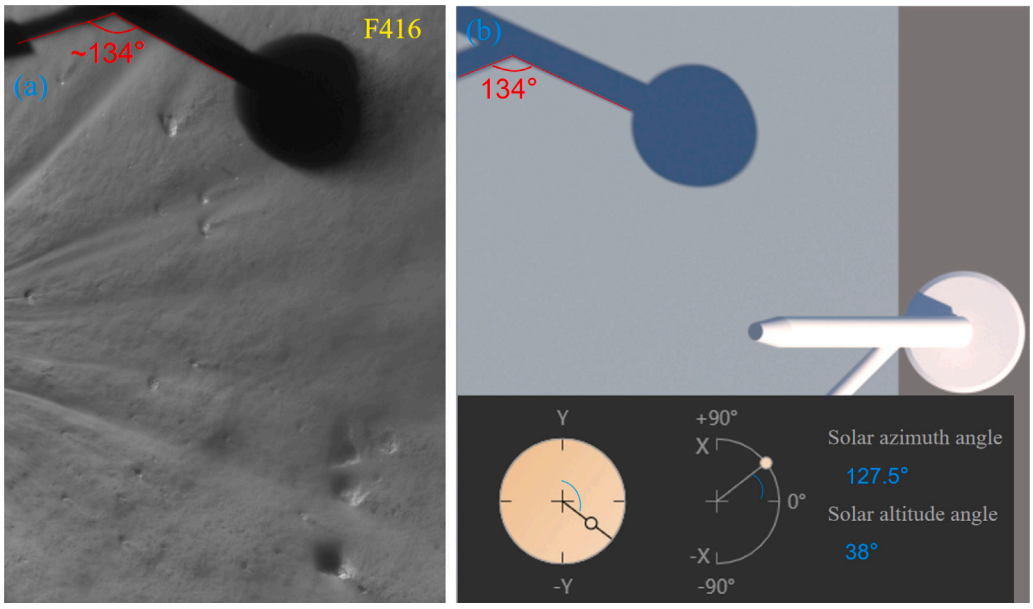

Fig. B.1. Matching diagram of solar azimuth and altitude angles when CE-5 landed. (a) CE-5 landing image 1 s before landing; the corresponding nozzle altitude is 1.54 m. The angle between the shadows of the shock-absorbing rods is 134°. (b) Extraction of solar azimuth and altitude angles based on the SketchUp software simulation of the shadow angle of the shock-absorbing rods.

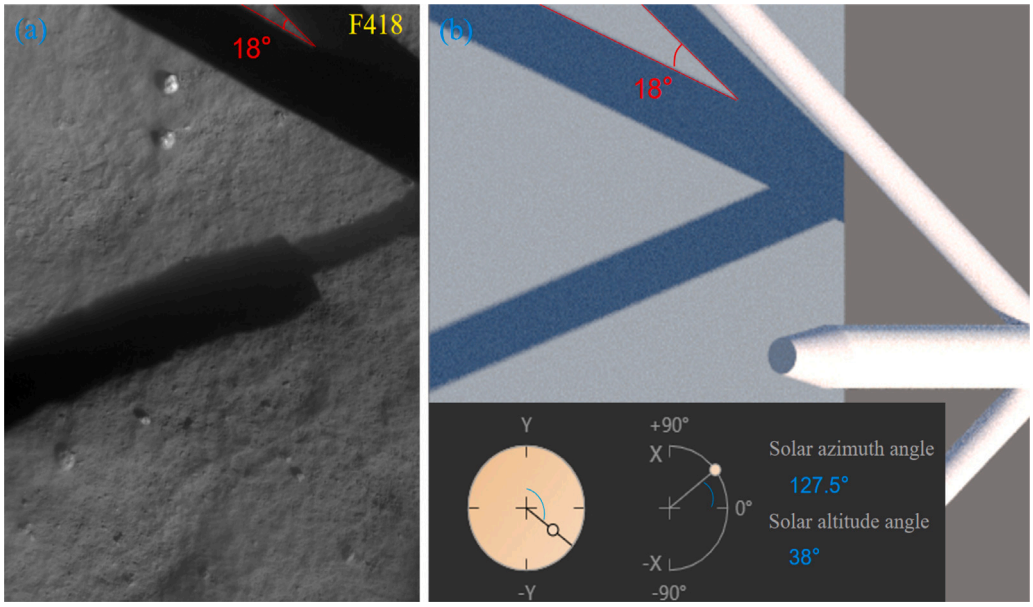

Fig. B.2. Matching diagram of the solar azimuth and altitude angles when CE-5 landed. (a) The CE-5 landing image 1 s after landing, the corresponding nozzle altitude is 0.46 m. The angle between the shadows of the shock-absorbing rods is 18°. (b) Extraction of the solar azimuth and altitude angles based on the SketchUp software simulation of the shadow angle of the shock-absorbing rods.

by the CE-5 landing camera. Based on the CE-5 landing images, we calculate the bulge thickness D_e as follows:

$$\begin{aligned}
\left(\frac{L}{D_e}\right)^2 &= \tan^2(\varphi) + \frac{1}{\tan^2(\angle D)} - 2\frac{\tan(\varphi)\cos(\angle E)}{\tan(\angle D)},\\
L &= \frac{h\times w}{F}\sqrt{\left(x_A - x_B\right)^2 + \left(y_A - y_B\right)^2},\\
\tan(\varphi) &= \frac{w\sqrt{(x_A-x_0)^2+(y_A-y_0)^2}}{F},\\
\cos(\angle E) &= \frac{\boldsymbol{e}_a\boldsymbol{e}_b}{|\boldsymbol{e}_a||\boldsymbol{e}_b|},\\
\boldsymbol{e}_a &= \left(x_A - x_0, y_A - y_0\right),\\
\boldsymbol{e}_b &= (-1, -\tan(\angle A)).
\end{aligned} \tag{C.1}$$

Here, the solar altitude angle $\angle D$ and azimuth angle $\angle A$ are equal to 38° and 127.5° respectively, which are from Appendix B. The camera altitude h is listed in Supplementary Table S1. The pixel size w, focal length F, and principal point coordinates (x_0, y_0) are the parameters of the CE-5 landing camera, which are listed in Supplementary Table S2. The pixel coordinates (x_A, y_A) and (x_B, y_B) correspond to the bulge vertex A and the corresponding projected point B in the landing image. Locations A and B are shown in Fig. C.1. The geometric meaning of the other quantities in Eq. (C.1) can also be found in this figure.

In the calculation of bulge thickness, we also estimate the uncertainty of the bulge thickness, which is caused by the uncertainty of the following input quantities: the solar altitude and azimuth angles, and the pixel coordinates of both the bulge vertex and its shadow on the lunar surface. Both the uncertainties of the solar altitude and azimuth angles are 1°. The uncertainties of other pixel coordinates are a single

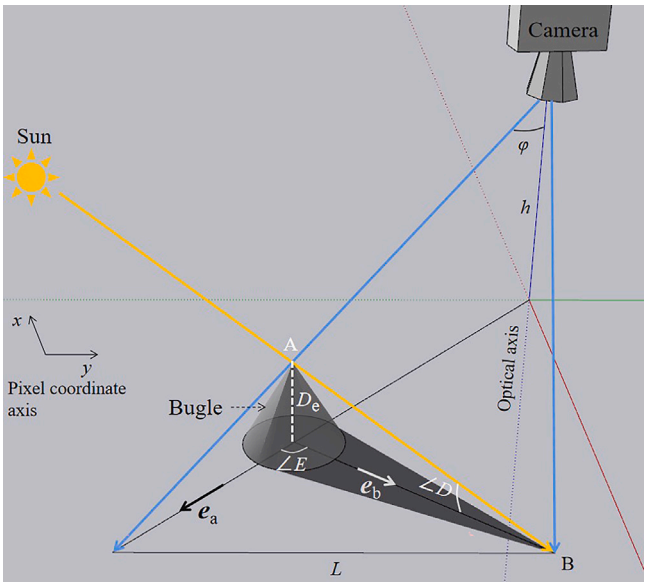

Fig. C.1. Geometry for calculating bulge thickness D_e. Point A is the bulge vertex, and point B is the corresponding projected point along the sunlight direction. $\angle D$ is the solar altitude angle. h is the camera height from the lunar surface. e_a, e_b, $\angle E$, and φ are calculated by using Eq. (C.1).

pixel. If the positions of both the bulge vertex and its shadow are ambiguous, the corresponding uncertainties are $n \geq 2$ pixels. Within a radius of n pixels, the pixel coordinates of the bulge vertex and its shadow are included.

Appendix D. Selecting lunar regolith bulges eroded by plumes

Fig. D.1(a) reveals 14 regolith bulges. The shapes of these bulges have been altered by plume erosion [see Fig. D.1(b)]. We calculate the heights of the bulges in Fig. D.1(a) and Fig. D.1(b). Their height difference is then regarded as the corresponding erosion depth. By using the method of Appendix C, we obtain the corresponding erosion depth (see points in the range 2–5 m in Fig. 4).

Appendix E. Threshold velocity formula and interparticle force

This appendix presents the threshold velocity formula for particle initiation under plume erosion and then obtains the interparticle force from this formula. Before presenting it, we introduce a formula for the threshold friction velocity of wind erosion. When gas flows horizontally over a soil surface, the particles on the top of the soil can be rotated about point P [Fig. E.1(a)]. During this rotation, the combined lifting effect of drag F_d and lift F_l overcome the combined retarding effect of particle gravity G and interparticle force F_i. The normal force between the bottom particles and the top particle and the interparticle force at point P are not presented in Fig. E.1(a) because the torque produced by these forces is zero when the top particle is rotating. The gas flow velocity u_* at which the particles start to move can be described by [20]

$$u_*^2 = f\left(Re_*\right)\left(\sigma_p g d + k\frac{6F_i}{\pi\rho_g d^2}\right), \tag{E.1}$$

where f is a function that depends on the particle Reynolds number at the threshold friction velocity, k is the ratio of r_i to r_l in Fig. E.1(a), σ_p, g, and d are the particle-to-gas density ratio, the gravitational acceleration, and the particle's diameter, respectively, and F_i and ρ_g are the interparticle force and gas density, respectively. Eq. (E.1) describes the threshold flow velocity of wind erosion for horizontal airflow.

However, Eq. (E.1) must be modified before applying it to plume erosion during landing. As shown in Fig. E.1(b), the lunar surface is subjected to plume pressure along the gravitational direction due to the impingement of the engine plume. The landing images from CE-4 and CE-5 also show that the lunar regolith is almost not eroded within r_0, where the top of the particle is subjected to the downward pressure P_d of the plume. Since the plume can also diffuse to the bottom of the particle, it exerts an upward pressure P_u on the bottom of the particle.

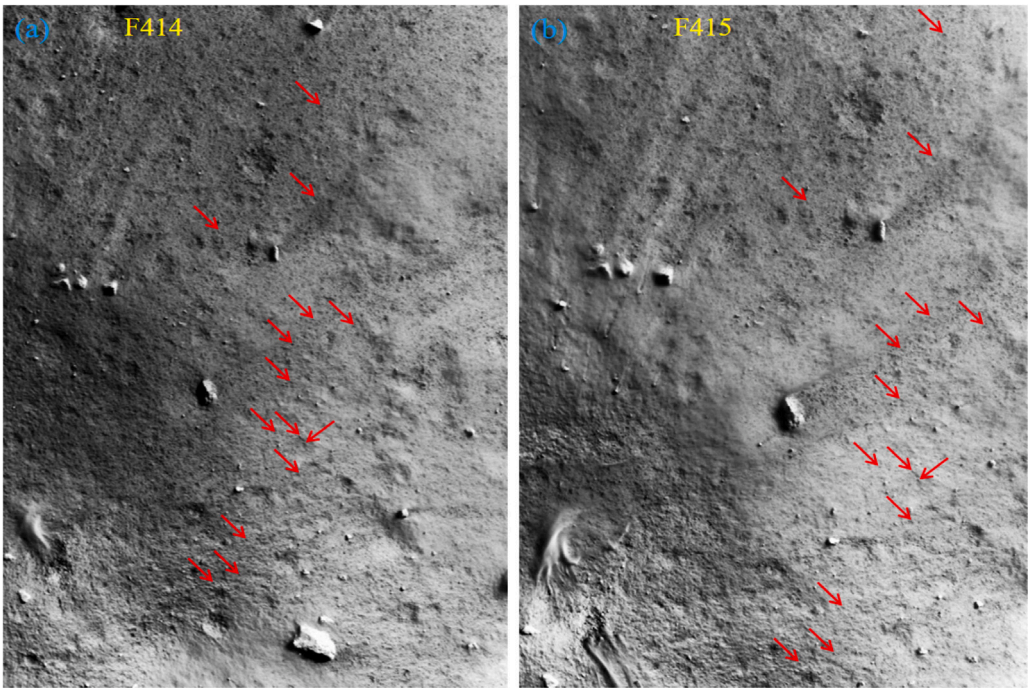

Fig. D.1. Comparison of erosion of regolith bulges (red arrows) in images F414 and F415. (a), (b) Images F414 and F415, corresponding to the 4th and 3rd second before landing, respectively. The arrows in these two images correspond one to one. The position indicated by the arrow is about 2–5 m from the nozzle axis. The contrast of images F414 and F415 is enhanced.

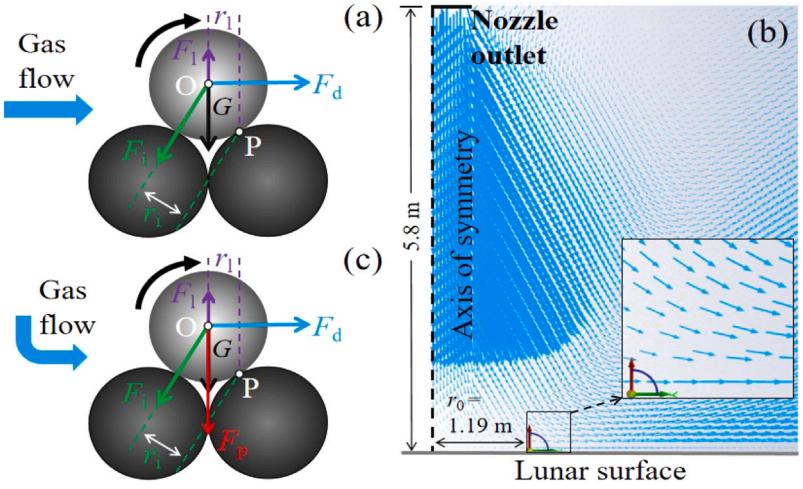

Fig. E.1. Schematic diagram of forces exerted on the particle due to wind erosion. (a) Horizontal gas flow erodes the particle on top of the soil. (b) Schematic diagram of the exhaust flow on the lunar surface. $r_0 = 1.19$ m corresponds to a nozzle altitude of 5.8 m for the CE-5 landing. (c) Schematic diagram of the forces exerted on the particle due to plume erosion associated with the position r_0. In panels (a) and (c), the forces exerted on the particle center of mass O are the interparticle force F_i, drag F_d, lift F_l of the gas flow, particle gravity G, and pressure F_p of the gas flow. Point P is a pivot. r_i and r_l are the moment-arm lengths associated with F_i and F_l, respectively.

Following a derivation similar to that of Shao and Lu [20], we derive the threshold velocity formula considering P_d and P_u of the plume:

$$u_*^2 = f\left(Re_*\right)\left[\left(\sigma_p g d + \frac{3\Delta P}{2\rho_g}\right) + k\frac{6F_i}{\pi\rho_g d^2}\right], \tag{E.2}$$

where $\Delta P = P_d - P_u$.

This paragraph summarizes the use of the erosion threshold equation. If the downward pressure of the plume on the particle is much greater than the upward pressure on the bottom of the particle, one obtains

$$\frac{1}{2}\rho_g u_*^2 \geq f\left(Re_*\right)\left[\left(\frac{1}{2}\rho_p g d + \frac{3}{4}P_d\right) + 3\sqrt{3}\frac{\beta}{\pi d}\right], \tag{E.3}$$

with $f(Re_*) = 0.026$ and $\beta = 8.45 \times 10^{-4}$ N/m to predict plume erosion. Based on Fig. 6, we can at least determine that the downward force of the plume plays an important role. Fig. 6 shows a continuous increase in dynamic pressure at r_0. Since the lunar regolith particles at r_0 are in a state of static equilibrium, they also need a continuously increasing external force to resist the increase in dynamic pressure. Only the friction induced by the downward force of the plume meets this condition. The action of dynamic pressure produces a friction force in the direction opposite the particle-slip direction, which is related to the downward force of the plume. When the nozzle height is reduced, the dynamic pressure and downward force of the plume at r_0 increase simultaneously. As a result, the lunar regolith particles at r_0 remain in a state of static equilibrium.

Appendix F. Calculation of drag coefficient

The drag coefficient C_d is computed based on the literature [26], which considers how compressibility and rarefaction affect drag. In the calculation of C_d, we add the missing term $2\sqrt{\pi}/3s$ to Eq. (25b) of Loth [26], and this term is from the literature [27], where s is the molecular speed ratio.

Appendix G. Supplementary data

Supplementary material related to this article can be found online at https://doi.org/10.1016/j.actaastro.2023.04.024.

References

[1] M.K. Barker, E. Mazarico, G.A. Neumann, et al., A new Lunar digital elevation model from the Lunar orbiter laser altimeter and SELENE Terrain camera, Icarus 273 (2016) 346–355.
[2] M.A. Wieczorek, G.A. Neumann, F. Nimmo, et al., The crust of the moon as seen by GRAIL, Science 339 (2013) 671–675.
[3] Q.L. Li, Q. Zhou, Y. Liu, et al., Two billion-year-old volcanism on the Moon from chang'E-5 basalts, Nature 600 (2021) 54–58.
[4] H. Tian, H. Wang, Y. Chen, et al., Non-KREEP origin for chang'E-5 basalts in the procellarum KREEP terrane, Nature 600 (2021) 59–63.
[5] S. Hu, H. He, J. Ji, et al., A dry Lunar mantle reservoir for young mare basalts of chang'E-5, Nature 600 (2021) 49–53.
[6] Z. Wang, Y. Wu, D.T. Blewett, et al., Submicroscopic metallic iron in Lunar soils estimated from the in situ spectra of the chang'E-3 mission, Geophys. Res. Lett. 44 (2017) 3485–3492.
[7] L.D. Jaffe, The surveyor Lunar landings: Landed spacecraft have returned much information about the surfaces of lunar maria and highlands, Science 164 (1969) 775–788.
[8] L. Roberts, The Action of a Hypersonic Jet on a Dust Layer, Institute of Aerospace Sciences 31st Annual Meeting, New York, 1963, IAS Paper No. 63.
[9] P.T. Metzger, J.E. Lane, C.D. Immer, Modification of roberts' theory for rocket exhaust plumes eroding lunar soil, in: Paper Presented At Proceedings of the 11th Biennial ASCE Aerospace Division International Conference on Engineering, Science, Construction, and Operations in Challenging Environments, California, United States, 2008.
[10] Y. Li, D. Ren, Z. Bo, et al., Gas-particle two-way coupled method for simulating the interaction between a rocket plume and Lunar dust, Acta Astronaut. 157 (2019) 123–133.
[11] A.B. Morris, D.B. Goldstein, P.L. Varghese, et al., Plume impingement on a dusty Lunar surface, AIP Conf. Proc. 1333 (2011) 1187–1192.
[12] A. Rahimi, O. Ejtehadi, K.H. Lee, et al., Near-field plume-surface interaction and regolith erosion and dispersal during the Lunar landing, Acta Astronaut. 175 (2020) 308–326.
[13] J. Lane, S. Trigwell, P. Hintze, et al., Further analysis on the mystery of the surveyor III dust deposits, in: Paper Presented At Proceedings of the 13th ASCE Aerospace Division Conference on Engineering, Science, Construction, and Operations in Challenging Environments, California, United States, 2012.
[14] C. Sagan, C. Chyba, Triton's streaks as windblown dust, Nature 346 (1990) 546–548.
[15] https://moon.bao.ac.cn/ce5web/moonGisMap.search.
[16] Y. Zheng, X. Deng, Z. Gu, et al., Lunar surface sampling point selection of chang'E 5, Opt. Precis. Eng. 29 (2021) 2935–2943.
[17] G.A. Bird, Molecular Gas Dynamics and the Direct Simulation of Gas Flows, Clarendon Press, Oxford, 1994.
[18] J. You, X. Zhang, H. Zhang, et al., Analysis of plume-Lunar surface interaction and soil erosion during the chang'E-4 landing process, Acta Astronaut. 185 (2021) 337–351.
[19] C. Li, H. Hu, M.F. Yang, et al., Characteristics of the Lunar samples returned by chang'E-5 mission, Natl. Sci. Rev. (2021) nwab188.
[20] Y. Shao, H. Lu, A simple expression for wind erosion threshold friction velocity, J. Geophys. Res. 105 (2000) 22437–22443.

[21] O.R. Walton, Review of adhesion fundamentals for micron-scale particles, Powder Part. J. 26 (2008) 129–141.
[22] V. Gromov, Physical and Mechanical Properties of Lunar and Planetary Soils, Vol. 236, Laboratory Astrophysics and Space Research. Astrophysics and Space Science Library, Springer, Dordrecht, 1999, pp. 121–142,
[23] P.T. Metzger, J. Smith, J.E. Lane, Phenomenology of soil erosion due to rocket exhaust on the Moon and the Mauna Kea Lunar test site, J. Geophys. Res. 116 (2011) E06005.
[24] A.B. Morris, D.B. Goldstein, P.L. Varghese, et al., Approach for modeling rocket plume impingement and dust dispersal on the Moon, J. Spacecr. Rockets. 52 (2015) 362–374.
[25] https://wgc.jpl.nasa.gov:8443/webgeocalc#IlluminationAngles.
[26] E. Loth, Compressibility and rarefaction effects on drag of a spherical particle, AIAA J. 46 (2008) 2219–2228.
[27] M. Parmar, A. Haselbacher, S. Balachandar, Improved drag correlation for spheres and application to shock-tube experiments, AIAA J. 48 (2010) 1273–1276.